Journal Pre-proof

Correlative surface and bulk analysis of deep cryogenic treatment influence on high-alloyed ferrous alloy

P. Jovičević-Klug, M. Jovičević-Klug, L. Tegg, D. Seidler, L. Thormählen, R. Parmar, M. Amati, L. Gregoratti, J.M. Cairney, J. McCord, M. Rohwerder, B. Podgornik

PII: S2238-7854(22)01783-5

DOI: https://doi.org/10.1016/j.jmrt.2022.11.075

Reference: JMRTEC 5974

To appear in: *Journal of Materials Research and Technology*

Received Date: 11 October 2022

Accepted Date: 11 November 2022

Please cite this article as: Jovičević-Klug P, Jovičević-Klug M, Tegg L, Seidler D, Thormählen L, Parmar R, Amati M, Gregoratti L, Cairney JM, McCord J, Rohwerder M, Podgornik B, Correlative surface and bulk analysis of deep cryogenic treatment influence on high-alloyed ferrous alloy, *Journal of Materials Research and Technology*, https://doi.org/10.1016/j.jmrt.2022.11.075.

Correlative surface and bulk analysis of deep cryogenic treatment influence on high-alloyed ferrous alloy

Jovičević-Klug, P.[1,2]*, Jovičević-Klug, M.[2], Tegg, L.[3,4], Seidler, D.[5], Thormählen, L.[5], Parmar, R.[6], Amati, M.[6], Gregoratti, L.[6], Cairney, J. M.[3,4], McCord, J.[5], Rohwerder, M.[2] and Podgornik, B.[1]

[1]Institute of Metals and Technology (IMT), Lepi pot 11, 1000 Ljubljana, Slovenia
[2]Max-Planck Institute für Eisenforschung GmbH, Max-Planck-Str. 1, 40237 Düsseldorf, Germany
[3]School of Aerospace, Mechanical and Mechatronic Engineering, The University of Sydney, Camperdown, NSW 2006, Australia
[4]Australian Centre for Microscopy and Microanalysis, The University of Sydney, Camperdown, NSW 2006, Australia
[5]Institute for Materials Science, Kiel University, Kaiserstraße 2, 24143, Kiel, Germany
[6]Elettra - Sincrotone Trieste, S.C.p.A., SS14 – km 163.5 in Area Science Park, 34149 Trieste, Italy

*Corresponding author: *Patricia Jovičević-Klug, ORCID 0000-0002-3758-9897, Institute of Metals and Technology, Lepi pot 11, 1000 Ljubljana, Slovenia and Max-Planck Institut für Eisenforschung, patricia.jovicevicklug@imt.si and p.jovicevic-klug@mpie.de, +49 211 6792 958*

Co-authors:

2. Matic Jovičević-Klug, ORCID 0000-0003-2783-4649, m.jovicevic-klug@mpie.de
3. Levi Tegg, ORCID 0000-0003-0496-8716, levi.tegg@sydney.edu.au
4. Dennis Seilder, ORCID 0000-0001-5817-3834, dese@tf.uni-kiel.de
5. Lars Thormählen, ORCID 0000-0002-9469-9961, lath@tf.uni-kiel.de
6. Rahul Parmar, ORCID 0000-0002-3439-7822; rahul.parmar@elettra.eu
7. Matteo Amati, ORCID 0000-0002-3809-2145; matteo.amati@elettra.eu
8. Luca Gregoratti, ORCID 0000-0002-4947-2370, luca.gregoratti@elettra.eu
9. Julie M. Cairney, ORCID 0000-0003-4564-2675, julie.cairney@sydney.edu.au
10. Jeffrey McCord, ORCID 0000-0003-0237-6450, jmc@tf.uni-kiel.de
11. Michael Rohwerder, ORCID 0000-0002-2466-3963, m.rohwerder@mpie.de
12. Bojan Podgornik, ORCID 0000-0002-3224-6449, bojan.podgornik@imt.si

Abstract

In this study we investigate the effect of deep cryogenic treatment (DCT) on a high-alloy ferrous alloy (HAFA) to understand the resulting chemical and physical changes to the HAFA's microstructure and properties. Using multiple materials analysis techniques, we uncover the fundamental chemical changes to the HAFA with DCT, and link changes in material properties to changes in the microstructure. The increased carbide nucleation with DCT is linked to greater solute mobility resulting from the modified stress state of the material and modified chemical bonding of the solutes with the matrix. In turn this provides the possibility of prior formation of nucleation points for primordial carbide formation that act as accelerators for both nucleation and evolution of carbides. These result in modified chemical and microstructural homogeneity of the material that fundamentally led to changes in the surface properties and applicability of HAFA in advanced wear, corrosion and fatigue resistance demanding conditions.

Keywords

nanoscopic chemistry, surface analysis, correlative analysis, magnetism, microstructure, deep cryogenic treatment

1. Introduction

Deep cryogenic treatment (DCT) has recently emerged as a cost-effective, green technology that affects both surface and bulk of a material or component[1]. DCT improves dimensional stability and mechanical properties of metallic materials by inducing changes in crystal structure[2], altering the residual stresses of the material[3,4], inducing the redistribution of atoms within the material [5] and creating at denser atomic structure[6]. In addition, DCT was observed also to increase Schottky barrier height (reduces material reverse leakage current)[7] and reduce free energy of crystals structure[8,9]. Subsequently, it can alter also magnetic properties[10], decrease hydrogen solubility[11] as well as altering binding energy of solute atoms in alloys[12]. It has been reported that DCT positively affects metallic materials' thermal conductivity[13,14], wear resistance[15–19], corrosion resistance[1,20,21] and oxidative resistance[1,12] and reduces friction[22,23], leading to prolonged lifetime of components[24,25]. These properties are particularly important for medical, energy sector, electronics and aerospace industry that utilize and expose materials in highly dynamic and demanding environments. In relation to this, DCT changes also bulk properties, which has been broadly reported to improve mechanical properties as well as fatigue resistance[26–28].

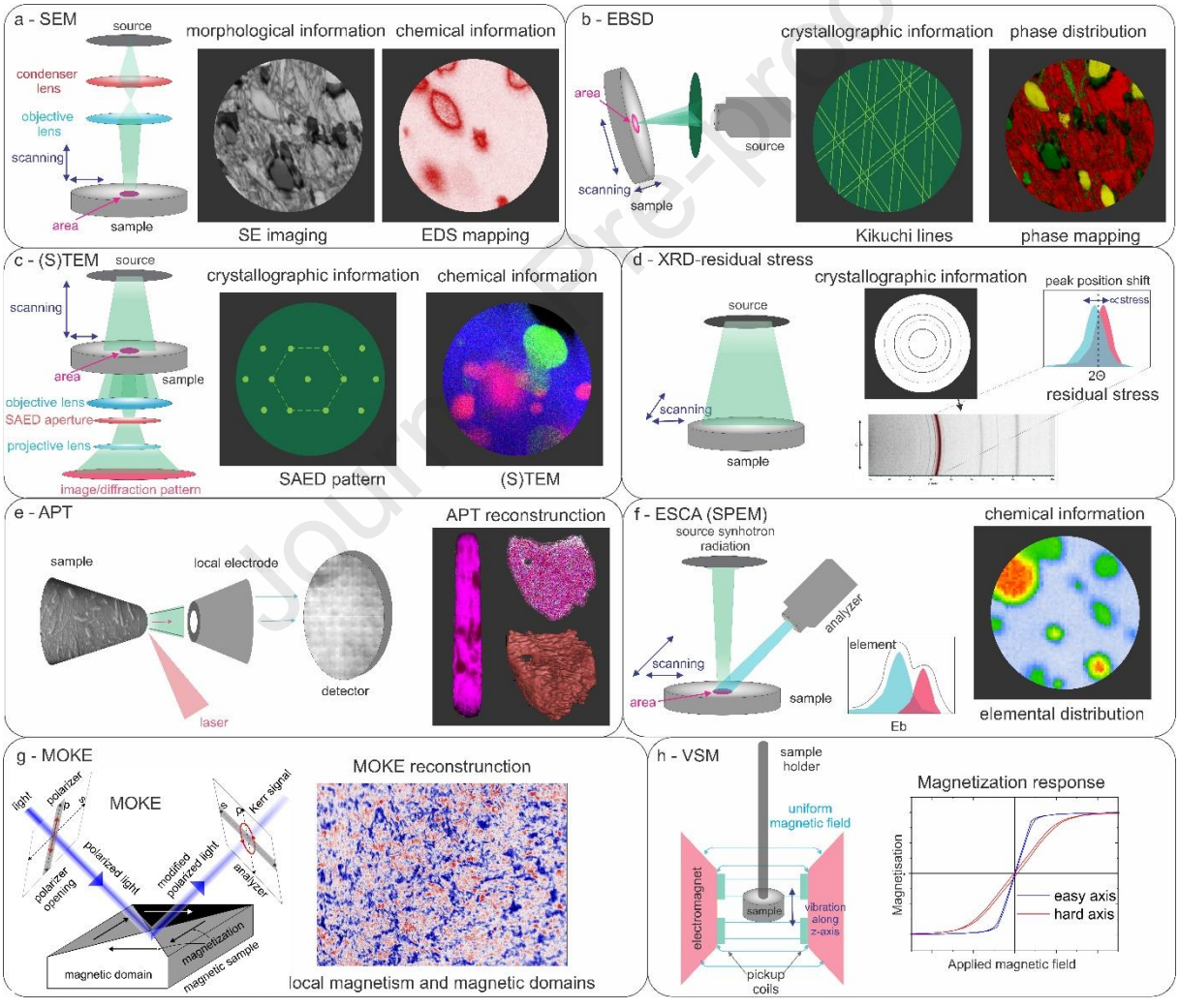

Figure 1: The representation of techniques used for correlative analysis from microstructure to surface and bulk analysis of samples.

The reported changes to material properties following DCT are associated with increased precipitation[29–31], a more homogenous microstructure[32,33] and changes to the matrix phase [15,34]. All these nanoscale and microscale changes impact the performance of material/component through changing their individual properties. The commonly accepted theories about DCT state that changes induced by internal stresses[35], the transformation of retained austenite into martensite [29–

31], and the increased driving force for carbide nucleation through lattice changes and accompanying dislocations, all lead to segregation of carbon and alloying elements and move them to close-by vacancies, which then act as the nucleation sites for newly formed carbides[25,36].

However, despite extensive research, there are many unsolved questions regarding the mechanisms behind DCT, particularly around surface chemistry and surface changes that are considered the main reasons for improved wear and corrosion resistance with DCT. As such, it is important to understand the underlying reasons for such changes in order to fully utilize DCT for advanced tailoring of surface-bound properties required for further improvement of materials. Additionally, the variations between differently alloyed and manufactured metallic materials have also not been characterized in depth and this has only started to be properly investigated within the last few years[25,34,37]. This has led to some contradictory results reported in the literature, and varying opinions on the effectiveness of DCT and its applicability for various metallic materials[24,25,36,38]. This has resulted in a poor utilization of DCT in industry as well as to a negligible effort in understanding the underlying mechanisms and effects of DCT on metallic materials and their properties.

Despite these setbacks, DCT has emerged within the last decade as a potential treatment that can be applied not only in specialized nanoscience and materials science applications, but also on a larger industrial scale such as in the tool and steel industry, automotive and music industry and many other industries[36]. The rise of DCT is also seeing the technique applied to other material platforms. This includes high-alloyed ferrous alloys[39], which use a variety of alloying elements in order to tailor microstructural properties (matrix, carbides)[40]. These alloys are commonly used in applications in high demanding environment at acceptable costs compared to other ferrous alloys. The main challenge of these alloys is their simultaneous improvement of wear, fatigue and corrosive properties, while also sustaining sufficiently high mechanical properties that are manipulated mostly with the formation of different carbide types through their morphology, chemistry and distribution[41]. As a result, to further optimize and manipulate these carbides and their precipitation, advanced heat treatment technologies such as DCT must be developed to overcome the reciprocal properties changes of such alloys obtained with conventional techniques.

In the present work, we investigated the effect of DCT on the surface and corresponding bulk properties of a highly-alloyed ferrous alloy (HAFA), EN HS6-5-2 (also known as AISI M35-high content of alloying elements) to answer existing questions about DCT and its effect on the treated material. Namely, the in-depth understanding of how DCT influences the bulk and surface properties of HAFA and how these relate to each other, with respect to the fundamental mechanisms of microstructural and chemical changes. Furthermore, the fundamental correlation between these two material aspects and their changes with DCT have to be resolved. With all of these insights, proper understanding of the DCT-induced phenomena can be provided, which essentially act as tools for advanced properties development of ferrous alloys that can be used in the most challenging environments, whilst delivering the necessary mechanical properties. For probing and understanding these aspects and relations several analytical techniques were used to study the bulk and surface microstructure and chemistry, as illustrated in Fig. 1. This ensemble of bulk and surface-sensitive techniques permitted novel correlative microscopy and microanalysis into the effect of DCT and its related phenomena. Furthermore, this unique correlative analysis provides an overall view of the DCT effect on HAFA ranging several length scales that also provide insight into the key probing capabilities of the methods for individual changes caused by DCT. With our research we thus provide a unique and in-depth view into the surface and bulk bound changes of HAFA with DCT and provide key aspects and reasons for DCT-induced changes and open a pathway towards novel tailoring and design of HAFA for advanced applications in challenging environments.

2. Methods

2.1. Material and heat treatment

Selected ferrous alloy was the wrought high-alloy ferrous alloy (HAFA) EN HS6-5-2 (also known as AISI M35), delivered in soft state by producer SIJ Metal Ravne, Ravne na Koroškem, Slovenia. The chemical

composition of HAFA is in wt.%, 0.90 C, 5.20 W, 4.10 Cr, 5.20 Mo, 2.01 V, 4.50 Co, 0.004 S, 0.34 Mn and Fe as base. All HAFA samples were firstly austenitized at 1230 °C for 2 mins in horizontal vacuum furnace IPSEN VTTC-324R (Ipsen, Kleve, Germany), followed by high-pressure gas quenching using N_2 at the pressure of 5 bars, where average quenching rate was about 7–8 °C s^{-1}. After quenching, HAFA samples were divided to two groups: control (conventionally heat-treated (CHT)) and test group (DCT). Selected heat treatment parameters were chosen based on our previous research of HAFA [1,12,32].

2.2. Microscopy and phase analysis and residual stress

Microstructural analysis of HAFA was obtained by using scanning electron microscope (SEM) Zeiss Crossbeam 550 FIB-SEM Gemini II (Oberkochen, Germany) at Max-Planck Institute for Iron Research, Düsseldorf, Germany and Institute of Metals and Technology, Ljubljana, Slovenia. Phase analysis of HAFA is based/provided by our previous study [32]. Residual stress analysis was conducted also at Max-Planck Institute for Iron Research at XRD Rikaku Smartlab 6KW (Tokyo, Japan), at 45 kv and 200 mA with scan range 0-45-90° with sample to detector distance 149.359 mm. The quantitative analysis of residual stress was performed with software Bruker Topas V5.0 (Billerica, MA, USA). Statistical evaluation of particles was conducted by SPSS, PASWStatistics18, SPSS Inc., (Chicago, IL, USA) and Origin version 2021, OriginLab Corporation (Northampton, MA, USA).

2.3. Scanning photoelectron microscopy

The scanning photoelectron microscopy (SPEM) was performed at the ESCA Microscopy beamline at the Elettra synchrotron radiation center by using the available special setup for cryogenic treatment (-140 °C) of samples; the base pressure of the microscope chamber was 3 x 10^{-10} mbar, photo energy of 750 eV and a photon energy of 750 eV was selected for the measurements. Samples were initially pre-quenched at Institute of Metals and Technology, and were then in-situ analyzed during the DCT (24 h) and tempering (1 x 550 °C / 2 for both samples) for both setups (CHT/DCT). Before the experiments, samples were ionically etched with Ar ions to remove unwanted oxide layer and surface contaminants. The cleanliness of each sample was thoroughly checked and no contaminants were spotted. The surface chemistry of samples was mapped with high spatial resolution and spectral surveys. The chemical surface maps of selected elements (C (C1s), Cr (Cr2p), Fe (Fe3p), Mo (Mo3d), V (V2p) and W (W4f)) were recorded. For a correct interpretation of the maps a subtraction of the topography signal was also done using well established procedures [42], so that the photoemission intensity maps represented the proper chemical contrast. The analysis of data was conducted by IgorPro8, WaveMetrics (Portland, OR, USA) and Origin, version 2021, OriginLab Corporation (Northampton, MA, USA).

2.4. Atom probe tomography

Specimens were prepared for atom probe tomography (APT) by electropolishing matchstick sections, first using 25% perchloric acid in glacial acetic acid with ≈ 15 V DC, then using 2% perchloric acid in 2-butoxyethanol at 5-10 V DC.[43] Atom probe tomography (APT) was performed using a Cameca LEAP4000XSi at School of Aerospace, Mechanical and Mechatronic Engineering, The University of Sydney. Specimens were analyzed at 50 K and evaporated in laser-pulsed mode with 150 pJ laser pulse energy and 200 kHz repetition rate. The standing voltage was controlled to result in a 2% detection rate with 57% detector efficiency. Data reconstruction was performed using AP Suite 6.2 [44].As no crystallographic poles were observed on the detector and the data collection ended without tip fracture, , the radius evolution was calculated from the standing voltage, and the image compression factor and field factor were estimated using post-mortem SEM images [43]. Analysis of the reconstruction was performed using the IVAS module of AP Suite 6.2. Cluster analysis of carbides was performed using the routines included within AP Suite, and considered clusters of C, C_3 and C_4 ions. The maximum separation d_{max} was chosen from the distance corresponding to the maximum difference between the observed nearest-neighbor distribution and that calculated by randomly assigning ionic identities. The minimum cluster size was set to eliminate the probability of a random cluster being included in the analysis. The erosion and envelope parameters were both set to $½d_{max}$.

2.5. Magneto-optical Kerr effect

For the magneto-optical (MOKE) investigation of the samples a modified upright high-resolution bright-field microscope Zeiss Axio Vario 2 with polarization optics, a blue LED light source with wavelength of 460 nm and an objective lens with the magnification of 100x and numerical aperture of 0.6 is utilized. The microscope setup includes a one-axis electromagnet with laminated FeSi yokes achieving homogeneous in plane fields of up to 150 mT for the specific sample dimensions and setup configuration. The MO sensitivity is set by positioning the light source in the back focal plane to an off-centre position to achieve longitudinal MO sensitivity[45]. To enhance the MO contrast differential imaging is used[46]. Further, to reduce the effects of sample shifts due to the applied external magnetic field, the images are acquired by switching from positive to negative fields as shown in[10].

2.6. Vibrating sample magnetometer

To determine the effects of the various temperature treatments on magnetic behavior, the above cylindrical solids were measured using a Lake Shore Cryotronics Type 7404 vibrating sample magnetometer (VSM). To determine the bulk magnetization, the VSM was calibrated with a Lake Shore nickel standard, model 730908, which has a magnetic moment of 6.92 mA/m² at room temperature and an applied magnetic field of 500 mT. The specimens, which were 5 mm in diameter and 2.5 mm high, were mounted with their tops on the specimen holder and the measurement of the specimens was made along the lateral surface of the cylinder. To achieve complete magnetic saturation of the samples, measurements were made in a field range from -1.7 T to 1.7 T with different increments between 60 mT and 8 mT.

3. Results and Discussion

3.1. Materials description: microstructure and residual stress analysis

The correlative microstructural analysis with SEM, (S)TEM, EBSD and APT showed distinctive differences between conventionally heat treated (CHT) and DCT HAFA samples. Based on our previous study[32] the selected HAFA consists of retained austenite (less than 1 vol.%), martensite and the carbides M_6C, M_2C and MC, regardless of heat treatment. Furthermore, SEM and EBSD analysis show that martensitic matrix in DCT sample is finer compared to CHT and that the martensitic laths are more oval and mostly aligned along [1 0 1] and [0 0 1], which is consistent with observations from a previous study[32]. On sub-microscopic level, detailed analysis of the precipitated carbides with SEM shows that the DCT sample has on average about 30% more sub-micrometer precipitated carbides compared to CHT, and a more homogenous distribution of them. Some of these carbides in the CHT sample were very large (up to 1 µm) with an additional group of carbides in the range of 100 nm or less. However, for the DCT sample, only the ≲100 nm carbides were found. Detailed carbide analysis (EDX and EBSD) (**Fig. 2a-b**) showed that M_6C type of carbide correspond to $Fe_3(Mo, W)_3C$ and the MC type to VC. XRD analysis before tempering in our last study[32] also showed the presence of M_2C carbide type corresponding to $(Fe, Mo, W, V)_2C$ (see **SM1**), which plays an important role in $M_{23}C_6$ carbides evolution.

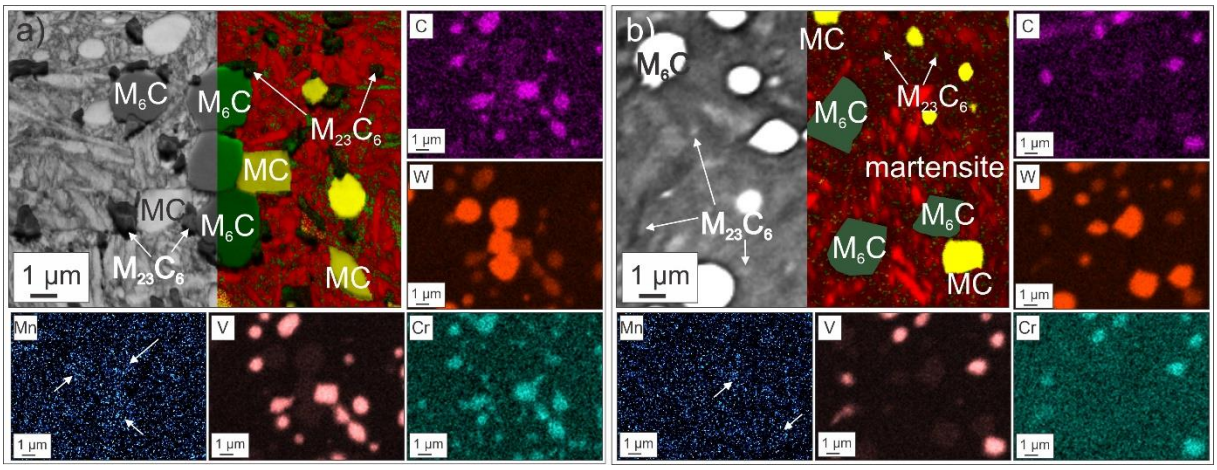

Figure 2: Results of EBSD analysis for a) CHT and b) DCT sample. Half of the image presents the grayscale secondary electron imaging contrast, whereas the other half represents the color-coded EBSD results (red-martensite, yellow-MC carbide, green-M_6C and $M_{23}C_6$ carbides). The surrounding monochromatic images represent individual elemental maps (marked in upper-left corner) acquired with EDX. For the Mn map, the white arrows indicate the positions of the M_6C carbides that show a slight enrichment in Mn.

Further analysis with TEM (**Fig. 3a-b**) and APT (**Fig. 4**) confirmed, regardless of heat treatment, also additional type of nanoscale carbides $M_{23}C_6$. The nanoscopic carbides $M_{23}C_6$ varied largely, some being larger than 20 nm while others were as small as ≈4 nm. The interesting observation was that smaller $M_{23}C_6$ carbides were positioned around bigger ones, which suggests there is an agglomeration process of smaller carbide to bigger $M_{23}C_6$. In addition, for both CHT and DCT samples twining of martensite was observed (**Fig. 3c**).

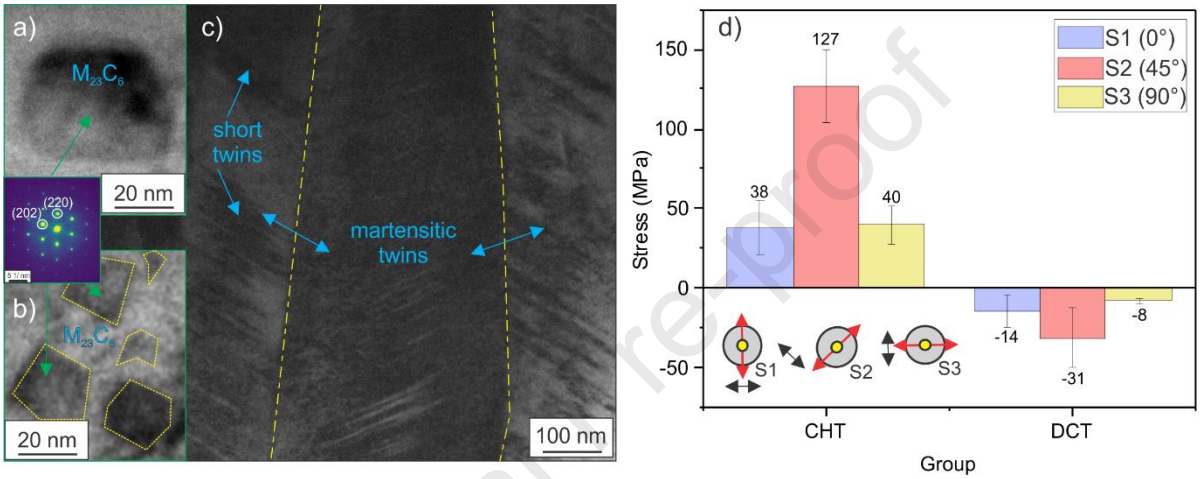

Figure 3: a-b) TEM analysis of $M_{23}C_6$ carbides, where a) corresponds to bigger $M_{23}C_6$ and b) to smaller $M_{23}C_6$ carbides, which form clusters. c) shows twinning of martensitic laths in DCT sample. d) Residual stress analysis of CHT and DCT sample, where S1 is in direction of 0°, S2 45° in and S3 90°, where S1 is in direction of 0°, S2 45° in and S3 90°.

In order to observe direct changes in microstructure in correlation to DCT, residual stress measurements were performed (**Fig. 3d**). Our results showed 78-85% less residual stress (depending on direction) in the DCT sample than the CHT sample. The DCT promotes the build-up of compressive stresses and release of tensile stresses compared to CHT. This can be directly linked to the increased transformation of retained austenite to martensite during DCT[4]. It should be noted that substantial relief of compressive residual stress can occur during tempering, as the samples were measured at final state after tempering. This stress relief results from the precipitation of finer carbides ($M_{23}C_6$)[47], and thus the changes in dimensional stability of martensite are enhanced by DCT[4]. As explained by Senthilkumar et al. 2011[4] , DCT at very low temperatures (-196 °C) promotes the development of compressive internal stresses, which cause crystal defects and thus changes the dimensional stability of martensite. This phenomenon then drives carbon and alloying elements (Cr, Mo, Fe, W etc.) to segregate at nearby defects, where first nuclei of carbides and then clusters of smaller carbides occur. This is consistent with the improved carbide evolution that was determined by APT and by spatially resolved SPEM measurements provided in the continuation of this article.

Though the analysis volumes are small (≈1.9×10^6 nm^3), APT analysis suggests the CHT sample has a larger population of $M_{23}C_6$ carbides. The likely reason of this is the higher number of larger ≈ 100 nm $M_{23}C_6$ carbides in DCT than in CHT, resulting in consumption of the nano-sized ones in their vicinity. Additionally, due to the more homogeneous microstructure after DCT than CHT, the localized inhomogeneities with CHT lead to a stronger variation in carbide nucleation and growth that can also contribute to a higher size divergence of precipitated carbides. This variation between samples is also supported by SEM and TEM observations. Selected-area electron diffraction in the TEM (**Fig. 3a-b**) reveals the $M_{23}C_6$ are FCC[32], and EDS (see **Fig. 2** and **SM2**) as well as APT (**Fig. 4**) suggest their

composition is Fe-based with enrichment of Cr, Co and Mn. Both TEM EDS and APT also indicate that in CHT $M_{23}C_6$ is Cr-enriched compared to DCT and that Mn can be also incorporated into the $M_{23}C_6$. This suggests that in addition to previously confirmed $M_{23}C_6$ type ($Fe_{21}Co_1Cr_1C_6$)[32] also more complex types in both CHT and DCT samples are present, such as $Fe_{21.5}(Cr,Mn)_{1.5}C_6$ for CHT and DCT, and perhaps the exclusive presence of $Fe_{21}Cr_2C_6$ for CHT (see also **SM2**). The formation of the specific types of carbides can consequently influence the final properties of the HAFA, such as corrosion, mechanical properties and magnetism[10,39,40].

In addition to $M_{23}C_6$, APT also confirmed the presence of carbides types M_7C_3 (higher alloying with Cr) and M_3C (higher alloying with Mo) for both CHT and DCT samples. M_7C_3 type of carbide is a type of HCP carbide[48] and its general chemistry corresponds to $(Cr,Mo)_7C_3$. M_3C is an orthorhombic type of carbide with chemical composition of $(Mo,Cr,V,W)_3C$, this type of carbide is known to be present in low Si HAFA[48]. These carbides are residual pieces of prior M_3C and M_2C carbides and are important in understanding how DCT modifies the microstructure. M_3C and M_2C carbides indicate that reactions of carbide evolution in both DCT and CHT are in-situ transformation of later types of carbides (M_3C/$M_2C \rightarrow M_7C_3 \rightarrow M_{23}C_6 \rightarrow M_6C$). This transformation also indicates in which crystal orientation direction the growth of carbide will occur[49]. Moreover, APT analysis indicates that also complex M_7C_3 carbides are present, which correspond to $(Cr,Mo\ Mn)_7C_3$, at which after DCT they appear slightly enriched with Mn compared to those after CHT. This is, similar to what was observed in our previous study for different type of HAFA[50]. As such, this mechanism of alloying segregation during DCT influences the local magnetic properties of the material, which can have a general effect on the overall bulk magnetic properties of the material, as discussed below.

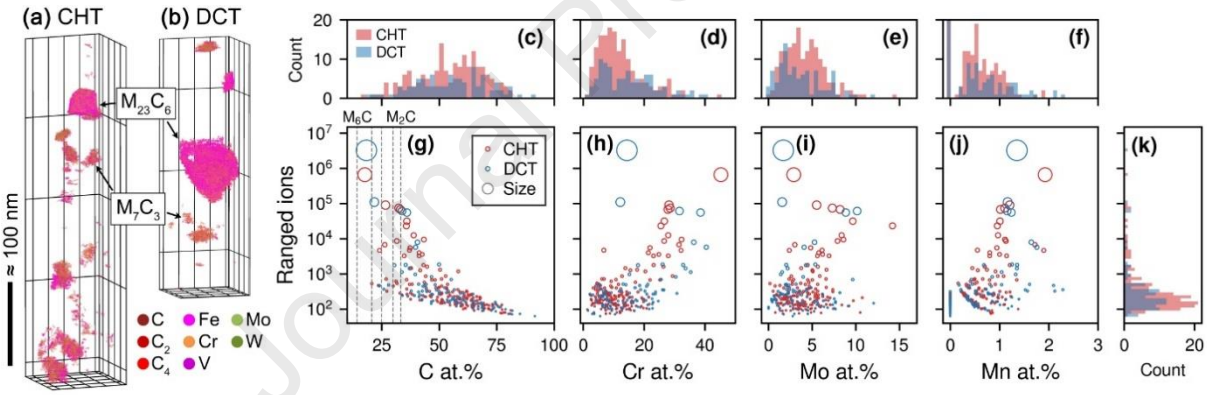

Figure 4: Carbide size and composition determined using cluster analysis of the atom probe tomography datasets. Note the scale bar is approximate as these datasets were not spatially calibrated[50]. (a,b) Reconstructed cluster positions for the CHT and DCT dataset showing selected ions. Large $M_{23}C_6$ and M_7C_3 clusters are labelled. (c–k) Histograms and scatter plots showing (c,g) C at.%, (d,h) Cr at.%, (e,i) Mo at.% and (f,j) Mn at.% with (g–j) the number of ranged ions in the cluster. (k) Shows a histogram of the number of ranged ions in each cluster. The circle size in (g–j) is also proportional to the number of ranged ions in the cluster. Dashed vertical lines in (g) indicate the C content of important carbides; from left-to-right these are M_6C, $M_{23}C_6$, M_3C, M_7C_3 and M_2C.

3.2. Chemical binding state changes with DCT

To understand the evolution and behavior of surface chemistry with DCT in comparison to CHT, we performed ex- and in-situ SPEM. From the SPEM chemical maps (**Fig. 5**) the positions of the major MC and M_6C carbides is revealed through their different V and W contents, respectively. The SPEM maps also unveil the strong changes that are caused by the tempering procedure for both samples (compare c) to d), e) to f) etc. in **Fig. 5**). The biggest change to the matrix relates to Cr and Mo (both red color-coded), which in both cases display a spatially uneven signal that is a result of the precipitation of $M_{23}C_6$ carbides. The Cr signal corresponds to the carbides, whereas the Mo primarily displays the resulting tempered matrix that is separated from the larger carbides and precipitated sub-micrometer carbides. In this sense, the Fe signal is not reliable in determining the carbides, since the $M_{23}C_6$ carbides form with a fraction of Fe within them, making the separation from matrix and carbide considerably weaker.

From the SPEM chemical maps the $M_{23}C_6$ carbides for the CHT variant are larger and more alloyed, whereas for the DCT samples they are considerably smaller and barely detectable due to their size ranging with the spatial resolution of the system. Nevertheless, in an overview manner the segmentation of the microstructure is visible for both samples.

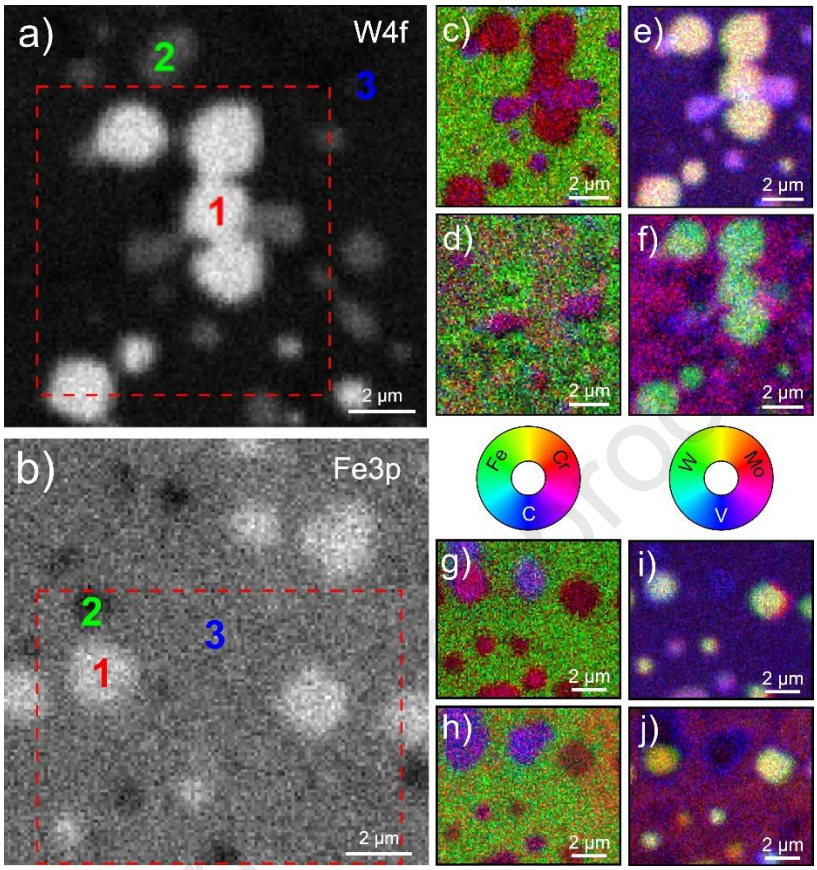

Figure 4: SPEM micrographs measured for a) CHT and b) DCT samples. The images c), e), g) and i) are obtained for samples after quenching and the images d), f), h) and j) were obtained for samples after tempering. The observational region for both samples is the same as the one investigated with SEM (**Fig. 2a-b**) The numbered positions correspond to selected positions traced with single-point XPS, the data of which is presented in Fig. 6 and **SM3-5**. c-j) color-coded composite SPEM images constructed from individual elemental SPEM maps, designated in the respective color wheels. The color wheels represent the base color mixture corresponding to individual ratio of the probed selected elemental signals with SPEM. The red dashed box in a) and b) represent the position of color-coded SPEM maps.

To extract more information about the Cr-rich $M_{23}C_6$ carbides, the Cr SPEM maps are reconstructed with focus on the binding energy range of metallic Cr (572-574 eV). This is done since the additional Cr-oxide signal related to localized oxidation of the surface can additionally contribute to the SPEM map without any connection to the carbides[50]. These maps (see **SM3**) indicate clearly a strong difference in the $M_{23}C_6$ carbide size between CHT and DCT, correlating well with the SEM results (**Fig. 2**). Additionally, the spatial distribution of the carbides is different. For CHT the carbides are mostly situated around larger carbides with a few smaller ones found within the matrix. In the DCT sample the carbides are more evenly distributed within the matrix, without displaying preference to the grain boundaries. The maps also interestingly display that the area coverage with $M_{23}C_6$ carbides is larger for the CHT sample compared to the DCT sample. However, this can be a misleading conclusion due to the smaller size of DCT carbides under the detection limit as well as due to the low signal to noise ratio that can result in a lower detection of the actual carbide fraction. For this reason, other techniques are required to assess such quantities in a more reliable manner, when the carbides size is below 100 nm size.

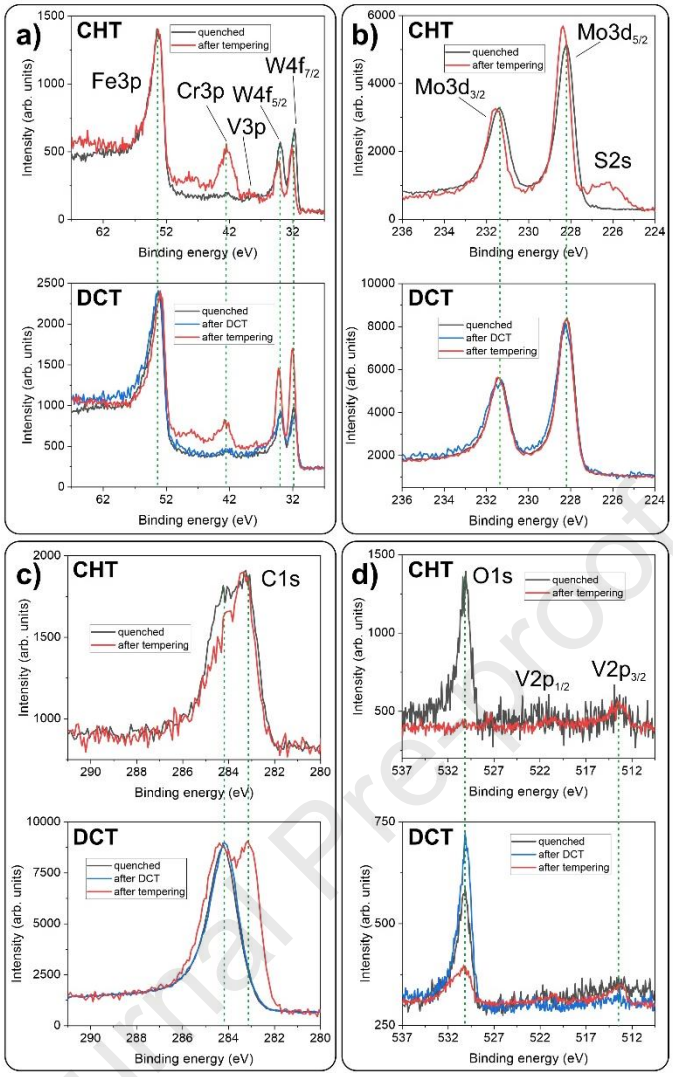

317

318 Figure 5: XPS spectra measured on the matrix position (position 3 in Fig. 5a-b) for CHT and for DCT
319 samples. The colored curves present the XPS spectra acquired at different sample states during their
320 processing. For direct comparison between CHT and DCT samples, the XPS spectra are grouped per
321 individual binding energy ranges to cover individual elemental peaks: a) Fe3p (53 eV), Cr 3p (42.5 eV),
322 V3p (38 eV) and W4f (34 eV and 32 eV); b) Mo3d (228 eV, 231.5 eV) and S2s (226.5 eV); c) C1s (284.5
323 eV); d) O1s (530 eV) and V2p (520.5 eV, 513.5 eV). The green dashed lines are provided as guidelines
324 for the assessment of peak shift from the initial position of individual XPS peaks.

325 The single-point analysis spectra in **Fig. 6** present the chemical changes of the matrix for both CHT and
326 DCT samples. The spectra in **Fig. 6a** indicate that for both CHT and DCT samples an increase in alloying
327 with Cr with respect to the Fe occurs with tempering. Additionally, the spectra also reveal a shift in the
328 W4f peaks by about 0.5 eV and 0.3 eV for CHT and DCT samples, respectively. A slight shift of 0.1 eV
329 is also registered for the Mo peaks for the CHT sample after tempering, while for DCT sample the shift
330 is not present (**Fig. 6b**). These shifts indicate a modified bonding of these alloying elements with Fe that
331 is postulated to result from the precipitation of $M_{23}C_6$ carbides. This is also seen in the XPS spectra of
332 the MC and M_6C carbides (**SM4** and **SM5**), at which the MC carbides display no specific Mo and W
333 shifts due to the low presence of Fe in such carbides. Interestingly, the DCT sample only shows a shift
334 in the Mo peak during the cooling part of the DCT for the matrix, whereas after tempering the Mo peak
335 is re-shifted to the same position as for the quenched state. This is consistent with our previous XPS
336 observations on a differently alloyed high-alloyed ferrous alloy[50]. This confirms that the same effect of
337 DCT on formation of Mo-rich primordial carbides, that act as nuclei for the M_7C_3 and $M_{23}C_6$ carbides, is
338 present also for this ferrous alloy. In combination with the previous observations as well as the
339 registration of the carbide form of C1s carbon (around 283 eV) in **Fig. 6c**, it is confirmed that the DCT
340 sample exhibits homogeneous nanoscopic carbide precipitation. This confirms the observations with
341 APT which also indicated a different chemical composition of the carbides for the CHT and DCT

samples, with a higher Cr and Mo content for the CHT carbides. Together with the Mo shift data, it is postulated that the CHT carbides are still in a stage with higher Mo content due to the missing boosted formation of the primordial carbides, whereas for DCT the carbides can evolve faster, leading to the formation of more evolved M_7C_3 and $M_{23}C_6$ carbides with lower Mo content. In addition, the changes in the chemical bonding also can explain the difference in the subsequent chemical composition of the precipitated carbides. It is proposed that due to the faster evolution of carbides and higher nucleation capabilities with DCT, the $M_{23}C_6$ carbides can form with lower incorporation of other, less common, alloying elements as defects due to the faster nucleation and evolution of carbides that suppresses the inhomogeneous alloying of carbides during their growth.

3.3. Magnetism

Both CHT and DCT samples were tested further in order to observe their magnetic behavior. With MOKE microscopy, the separation of the matrix (predominantly blue) from the carbides (predominantly white and red) via their magnetic contrast is achieved (**Fig. 7a-b**). The micrographs of the correlative site confirm the arrangement of the carbides within the matrix disclosed by other methods. The smaller-sized precipitated carbides are only visible for the CHT sample, since the DCT $M_{23}C_6$ carbides are smaller than the resolution limit of the microscope, as explained in the section on microstructure.

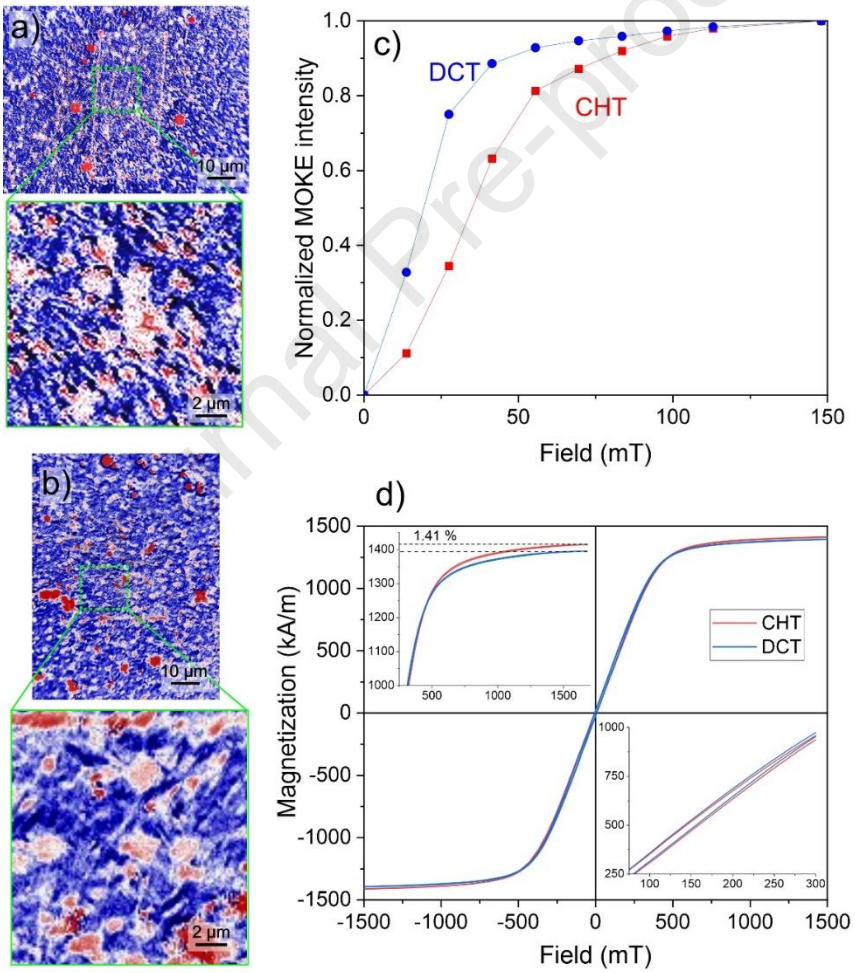

Figure 6: MOKE micrographs with enlarged regions of interest for a) CHT and b) DCT sample. c) Diagram of normalized MOKE signal intensity versus applied external magnetic field extracted from the larger MOKE micrographs of the same sample area exposed to different magnetic fields. d) magnetization hysteresis of CHT and DCT sample measured with VSM.

The average size of the martensitic laths and their morphology appear similar for both CHT and DCT samples. The major difference between the samples is revealed through successive application of an increasing external magnetic field (see **SM6**) that discloses a faster magnetization change for the DCT sample over the CHT sample. The normalized Kerr intensity (Fig. 7c) reveals that the magnetization

predominantly switches faster for the DCT throughout the entire field range, indicating a magnetically softer behavior of the surface of the DCT sample. This is further supported by VSM measurements (Fig. 7d) that additionally confirm the faster magnetization increase for the DCT sample in the initial part of the hysteresis curve. However, the VSM data also indicates that the magnetic moment is lower for the DCT sample compared to its CHT counterpart by 1.33%. The increased magnetic response of the DCT sample over its CHT variant is considered to occur due to the lower stress state of the DCT sample as indicated from the stress measurements. This is further supported by our previous study[10] in which the local magnetic response for multiphase high-alloyed ferrous alloy can be correlated to the residual state of the material. In relation to the magnetization reduction with DCT, it is postulated that the increased volumetric fraction of precipitated carbides causes a reduction in the overall magnetization of the ferrous alloy. This is further supported by comparing the extracted volumetric fraction of the carbide fractions from previous research[23] that falls within the 1% uncertainty range of X-ray diffraction (XRD).

Due to the high sensitivity of VSM to modification of phase fractions and magnetic properties of phases, very small phase changes can be detected[51]. However, the data interpretation is not trivial, when considering that magnetic moment changes with the different carbide structures as well as with the de-alloying of the matrix with carbide precipitation. The carbides, when assuming only precipitation of $M_{23}C_6$ variants, still hold a significant amount of net magnetic moment, resulting in a saturation magnetization in the order of 700-900 kA/m[52] about 2-2.5 times less than iron[53]. Fortunately, the carbides are completely separated phases from the matrix with strong incoherent grain boundaries, making them behave like isolated voids in correlation to the matrix material and internal magnetic flux. As a result, the magnetic flux preferentially flows through the matrix due to its higher permeability than of the carbides, leading to the saturation of the matrix with moderate fields without complete saturation of the carbides. With this , the volumetric fraction of the carbides can be assumed from the difference between the quasi-saturation magnetization of the matrix part and the magnetic saturation of pure iron (~1715 kA/m)[53]. With the measured maximum saturations of 1415 k/Am and 1395 k/Am we can calculate the volumetric fraction of carbides to be 17.49% and 18.65% for CHT and DCT, respectively. The values fall in the range of the expected carbide fraction that was determined from XRD and SEM analysis[23], validating the proposed assumptions. The slightly higher values compared to the XRD and SEM results are associated with the capabilities of magnetic measurements to be sensitive to even nanoscale formation of precipitates, whereas the probing capabilities of other techniques have a larger uncertainty in the nanometer scale and when the fractions of phases are low. As a result, VSM delivers great insight into the carbide precipitation modification with DCT and indeed confirms a higher fraction of carbides compared to the CHT counterpart. However, since the different types of carbides cannot be separated, the method only delivers an absolute difference in the total carbide volumetric fraction. For this reason, the microscopy studies (such as SEM, TEM and APT) are still necessary to probe the quantities of different carbide species. Furthermore, these assumptions for carbides only hold when also the austenite fraction and other non-magnetic phases are considered and evaluated with other techniques such as XRD. For the selected ferrous alloy of this study, the values of these phases are well under 1 vol.%[10,32] and can be disregarded in our case.

4. Conclusions

To summarize, this study demonstrates that DCT not only alters the microstructure of HAFA, but also it is an effective technique to change the residual stress and magnetic response of HAFA. Furthermore, the study also provides fundamental understanding of DCTs mechanism and the formation of nanoscale $M_{23}C_6$ carbides using scanning and transmission electron microscopy (SEM/TEM), atom probe tomography (APT) and scanning photoelectron microscopy (SPEM) that stem from nanoscale chemical as well as microstructural changes. These techniques allowed ex- and in-situ observation of the simultaneous formation of different regions of $M_{23}C_6$ carbides and preferential alloying elements dynamics during DCT and tempering. With such fundamental insight it is now clear that the nanoscale alloying dynamics related to carbide nucleation and formation play an essential role in the changes of the solute atoms binding with the matrix that modify its chemical and microstructural state on a microscopic to macroscopic scale. As such the DCT-induced chemical changes have a direct effect on

the bulk and surface properties of the material and with this the capabilities of the material to withstand different environments and conditions. As such we provide the initial stepping stone from a fundamental and phenomenological point of view for optimal utilization of DCT for advanced materials properties development, where surface characteristics play a decisive role.

CRediT authorship contribution statement

P.J.-K.: Conceptualization, Methodology, Investigation, Visualization, Writing-Original Draft, Writing-Editing and Review.
M.J.-K.: Methodology, Investigation, Visualization, Writing-Original Draft, Writing-Editing and Review.
Le.Te.: Methodology, Investigation, Visualization, Writing-Original Draft, Writing-Editing and Review.
D.S.: Methodology, Writing-Original Draft, Writing-Editing and Review
La.Th.: Methodology, Writing-Original Draft, Writing-Editing and Review
R.P.: Methodology, Writing-Editing and Review.
M.A.: Methodology, Writing-Editing and Review.
L.G.: Methodology, Writing-Editing and Review.
J.M.C.: Supervision, Resources, Writing-Editing and Review.
J.M.: Supervision, Resources, Writing-Editing and Review.
M.R.: Supervision, Resources, Writing-Editing and Review.
B.P.: Supervision, Resources, Writing-Editing and Review.
All authors have read and agreed to the published version of the manuscript.

Funding: This work was supported by Slovenian Research Agency (ARRS), Ljubljana, Slovenia [No. P2-0050]. Authors P.J-K., M.J-K. and B.P. would like to acknowledge Elettra Synchrotron Trieste for providing access to its synchrotron radiation facilities and for financial support of project 20215763. Authors L.T. and J.M.C. would like to acknowledge the Australian Research Council (ARC) [Future Fellowship FT180100232].

Acknowledgement: The authors acknowledge the technical and scientific assistance of Institute of Metals and Technology, Slovenia, Elettra Synchrotron Trieste, Italy, Max-Planck-Institute für Eisenforschung, Germany and Sydney Microscopy & Microanalysis, the University of Sydney node of Microscopy Australia.

Author statement: The authors declare no competing interests.

Data availability: The raw/processed data required to reproduce these findings cannot be shared at this time as the data also forms part of an ongoing study.

References

[1] P. Jovičević-Klug, M. Jovičević-Klug, B. Podgornik, Coatings 12 (2022) 213.
[2] D. Senthilkumar, Materials and Manufacturing Processes 29 (2014) 819–825.
[3] D. Senthilkumar, Advances in Materials and Processing Technologies 2 (2016) 427–436.
[4] D. Senthilkumar, I. Rajendran, M. Pellizzari, J. Siiriainen, J Mater Process Technol 211 (2011) 396–401.
[5] A. Levy, J.M. Papazian, Journal of Engineering and Technology 115 (1993) 129–133.
[6] L. He, Z.Q. Shi, Solid State Electron 39 (1996) 1811–1815.
[7] Z.Q. Shi, R.L. Wallace, W.A. Anderson, Appl Phys Lett 59 (1991) 446–448.
[8] H. huai Liu, J. Wang, B. luo Shen, H. shan Yang, S. ji Gao, S. jiu Huang, Mater Des 28 (2007) 1059–1064.
[9] F. Diekman, in: J. Dossett, G.E. Totten (Eds.), Steel Heat Treating Fundamentals and Processes-ASM Handbook, ASM International, Cleveland, OH, USA, 2013, pp. 382–386.
[10] M. Jovičević-Klug, P. Jovičević-Klug, J. McCord, B. Podgornik, Journal of Materials Research and Technology 11 (2021) 1245–1259.
[11] K. Bán, A. Lovas, L. Novák, K. Csach, Czechoslovak Journal of Physics 54 (2004) 12–15.
[12] P. Jovičević-Klug, M. Jenko, M. Jovičević-Klug, B. Šetina Batič, J. Kovač, B. Podgornik, Appl Surf Sci 548 (2021) 1–11.
[13] N.A. Özbek, A. Cicek, M. Gülesin, O. Özbek, P. Chen, T. Malone, P. Torres, R. Bond, O. Senkov, S. Senkova, A.L. Woodcraft, W.S. Lee, C.R. Lin, D.H. Park, S.W. Choi, J.H. Kim, J.M. Lee, M. Kumar, N. Sotirov, F. Grabner, R. Schneider, G. Mozden, S. Budurov, S. Yaneva, N. Stoichev, P. vân Bá, Y.B. Lee, D.H. Shin, K.T. Park, W.J. Nam, A. Molinari, I. Lonardelli, K. Demetrio, C. Menapace, V.F. Steier, E.S.

Ashiuchi, Reissig. L., J.A. Araujo, M. Levine, C. White, Y.T. Lin, M.C. Wang, Y. Zhang, Y.Z. He, D.P. Wang, Y. Wang, Z. Jiang, O. Senkov, S. Senkova, Cryogenics (Guildf) 146 (2004) 44–58.
[14] M. Baruci, L. Risegari, E. Olivieri, E. Pasca, G. Ventura, Astroparticle, Particle and Space Physics, Detectors and Medical Physics Applications (2004) 541–545.
[15] B. Podgornik, D. Uršič, I. Paulin, International Journal of Microstructure and Materials Properties 12 (2017) 216.
[16] D. Das, A.K. Dutta, K.K. Ray, Wear 267 (2009) 1371–1380.
[17] J. Li, X. Yan, X. Liang, H. Guo, D.Y. Li, Wear 376–377 (2017) 1112–1121.
[18] A. Akhbarizadeh, A. Shafyei, M.A. Golozar, Mater Des 30 (2009) 3259–3264.
[19] E.R. Fábián, L. Tóth, C. Huszák, Acta Materialia Transylvanica 2 (2019) 87–92.
[20] M. Jovičević-Klug, P. Jovičević-Klug, T. Kranjec, B. Podgornik, Journal of Materials Research and Technology 14 (2021) 2365–2381.
[21] J. Voglar, Ž. Novak, P. Jovičević-Klug, B. Podgornik, T. Kosec, Metals (Basel) 11 (2020) 14.
[22] N.W. Khun, E. Liu, A.W.Y. Tan, D. Senthilkumar, B. Albert, D. Mohan Lal, Friction 3 (2015) 234–242.
[23] P. Jovičević-Klug, G. Puš, M. Jovičević-Klug, B. Žužek, B. Podgornik, Materials Science and Engineering: A 829 (2022) 142157.
[24] D. Senthilkumar, in: G.E. Totten, R. Colas (Eds.), Encyclopedia of Iron, Steel, and Their Alloys, Taylor and Francis: NY, USA, New York, NY, 2016, pp. 995–1007.
[25] P. Baldissera, C. Delprete, The Open Mechanical Engineering Journal 2 (2008) 1–11.
[26] P. Baldissera, C. Delprete, Cryogenic Treatment and Fatigue Resistance, 2011.
[27] D. Korade, K.V. Ramana, K. Jagtap, Transactions of the Indian Institute of Metals 73 (2020) 843–851.
[28] A. Bensely, L. Shyamala, S. Harish, D. Mohan Lal, G. Nagarajan, K. Junik, A. Rajadurai, Mater Des 30 (2009) 2955–2962.
[29] L. Tóth, 3 (2018) 1–7.
[30] P. v Krot, S. Bobyr, N. v Biba, (2016).
[31] P. Jurči, J. Ptačinová, M. Sahul, M. Dománková, I. Dlouhy, Matériaux and Techniques 106 (2018) 104–113.
[32] P. Jovičević-Klug, M. Jovičević-Klug, B. Podgornik, Journal of Materials Research and Technology 9 (2020) 13014–13026.
[33] A. Antony, N.M. Schmerl, A. Sokolova, R. Mahjoub, D. Fabijanic, N.E. Stanford, Metals 2020, Vol. 10, Page 1561 10 (2020) 1561.
[34] P. Jovičević-Klug, M. Jovičević-Klug, T. Sever, D. Feizpour, B. Podgornik, Journal of Materials Research and Technology 14 (2021) 1007–1020.
[35] D.N. Collins, Heat Treatment of Metals 23 (2010) 40–42.
[36] P. Jovičević-Klug, B. Podgornik, Metals (Basel) 10 (2020) 434.
[37] P. Jovičević-Klug, A.Z. Guštin, M. Jovičević-Klug, B. Šetina Batič, A. Lebar, B. Podgornik, Journal of Materials Research and Technology 18 (2022) 3184–3197.
[38] M. Vengatesh, R. Srivignesh, T. Pradeep, N.R. Karthik, International Research Journal of Engineering and Technology 3 (2016) 417–422.
[39] A. Schulz, V. Uhlenwinkel, C. Escher, R. Kohlmann, A. Kulmburg, M.C. Montero, R. Rabitsch, W. Schützenhöfer, D. Stocchi, D. Viale, Materials Science and Engineering: A 477 (2008) 69–79.
[40] K.C. Hwang, S. Lee, H.C. Lee, Materials Science and Engineering: A 254 (1998) 282–295.
[41] C. Rodenburg, W.M. Rainforth, Acta Mater 55 (2007) 2443–2454.
[42] L. Gregoratti, M. Marsi, G. Cautero, M. Kiskinova, G.R. Morrison, A.W. Potts, Nuclear Instruments and Methods in Physics Research A (2001) 884–888.
[43] B. Gault, M.P. Moody, J.M. Cairney, S.P. Ringer, Atom Probe Microscopy, Springer New York, New York, NY, 2012.
[44] D.A. Reinhard, T.R. Payne, E.M. Strennen, E. Oltman, B.P. Geiser, G.S. Sobering, J. Mandt, Microscopy and Microanalysis 25 (2019) 302–303.
[45] J. McCord, J Phys D Appl Phys 48 (2015) 333001.
[46] F. Schmidt, W. Rave, A. Hubert, IEEE Trans Magn 21 (1985) 1596–1598.
[47] J.Y. Huang, Y.T. Zhu, X.Z. Liao, I.J. Beyerlein, M.A. Bourke, T.E. Mitchell, Materials Science and Engineering A 339 (2003) 241–244.
[48] R.A. Mesquita, H.J. Kestenbach, in: Solid State Phenomena, Trans Tech Publications Ltd, 2011, pp. 414–419.
[49] A. Inoue, T. Masumoto, Carbide Reactions (M3C->M703->M2306->M6 C) During Tempering of Rapidly Solidified High Carbon Cr-W and Cr-Mo Steels, n.d.
[50] P. Jovičević-Klug, L. Tegg, M. Jovičević-Klug, R. Parmar, M. Amati, L. Gregoratti, L. Almasy, J.M. Cairney, B. Pogornik, In Progress. (2022).
[51] Y. Yurekturk, M. Baydogan, Materials Science Forum 907 (2017) 50–55.
[52] T.P. Hou, K.M. Wu, W.M. Liu, M.J. Peet, C.N. Hulme-Smith, L. Guo, L. Zhuang, Scientific Reports 2018 8:1 8 (2018) 1–10.
[53] J. Crangle, G.M. Goodman, Proc R Soc Lond A Math Phys Sci 321 (1971) 477–491.

533

534 **Supplementary material 1:** Individual elemental maps (marked in upper-right corner) acquired with
535 EDX for a) CHT and b) DCT sample.

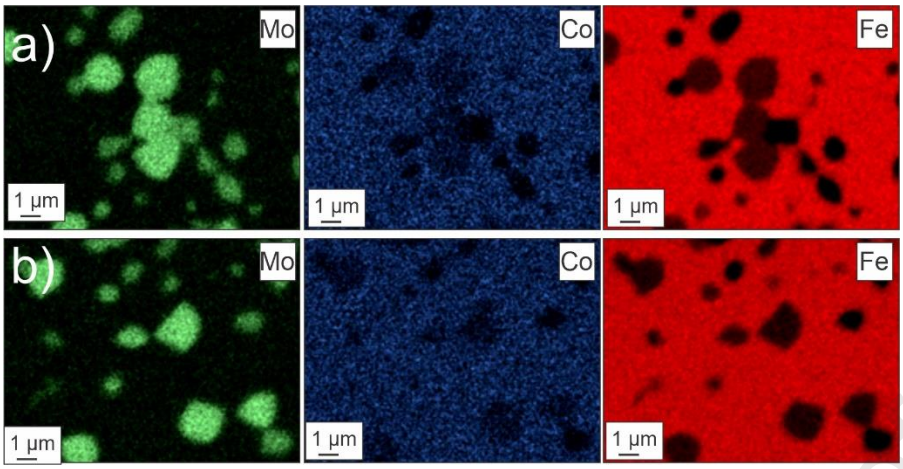

536

537

Supplementary material 2: Exemplar TEM images of precipitated carbides (marked with red arrows) in CHT and DCT samples. In the table below the EDX measured chemical composition (in at.%) of representative carbides for both samples is presented. The terms smaller and larger correspond to carbides to size of around 30-80 nm and 80-200 nm, respectively.

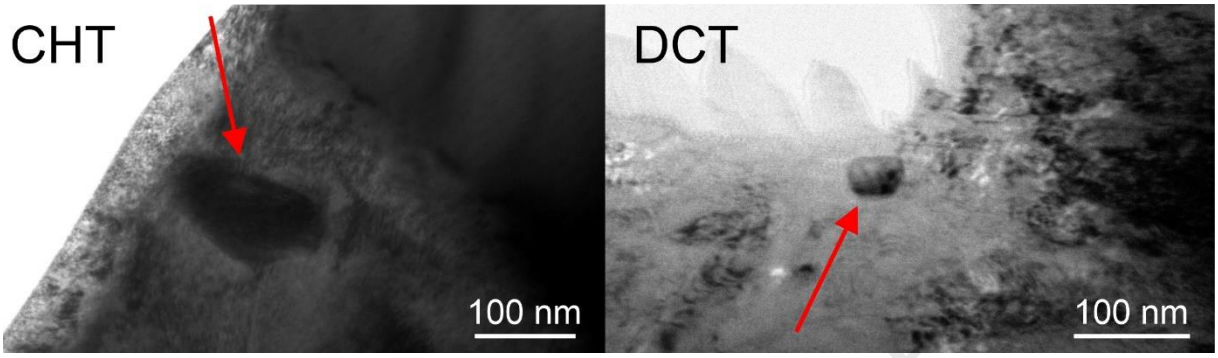

Sample	C	V	Cr	Mn	Fe	Co	Mo	W
CHT - larger	**19.72**	**0.67**	**4.23**	**0.68**	**69.83**	**2.33**	**1.69**	**0.84**
CHT - smaller	**14.21**	**1.07**	**3.82**	**1.00**	**76.87**	**0.27**	**1.86**	**0.91**
DCT - larger	**22.68**	**0.87**	**3.42**	**1.09**	**65.12**	**4.05**	**2.01**	**0.76**
DCT - smaller	**13.36**	**0.81**	**3.73**	**1.36**	**78.07**	**0.65**	**1.41**	**0.60**

544 **Supplementary material 3:** SPEM micrographs for metallic Cr3p for CHT and DCT, colour coded with
545 orange representing high signal and purple/white low signal.

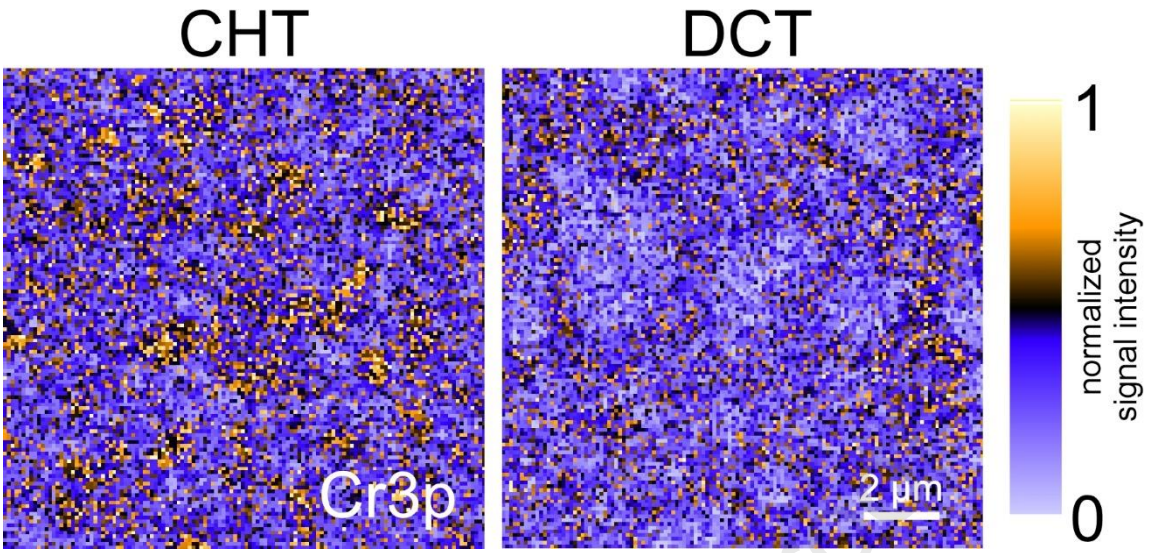

546

547

548

549

Supplementary material 4: XPS spectra measured on the MC carbide position (position 2 in Fig. 5a-b) for CHT (above) and DCT (below) samples. The coloured curves present the XPS spectra acquired at different sample states during their processing. For direct comparison between CHT and DCT samples, the XPS spectra are grouped per individual binding energy ranges to cover individual elemental peaks: from left to right Fe3p (53 eV), Cr 3p (42.5 eV), V3p (38 eV) and W4f (34 eV and 32 eV); Mo3d (228 eV, 231.5 eV) and S2s (226.5 eV); C1s (284.5 eV); O1s (530 eV) and V2p (520.5 eV, 513.5 eV).

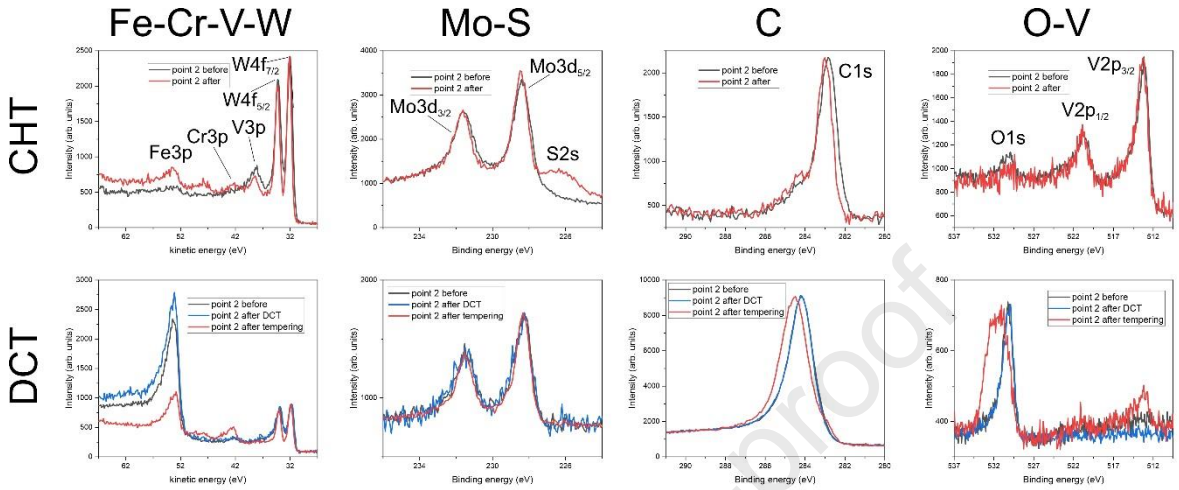

Supplementary material 5: XPS spectra measured on the M_6C carbide position (position 1 in Fig. 5a-b) for CHT (above) and DCT (below) samples. The coloured curves present the XPS spectra acquired at different sample states during their processing. For direct comparison between CHT and DCT samples, the XPS spectra are grouped per individual binding energy ranges to cover individual elemental peaks: from left to right Fe3p (53 eV), Cr 3p (42.5 eV), V3p (38 eV) and W4f (34 eV and 32 eV); Mo3d (228 eV, 231.5 eV) and S2s (226.5 eV); C1s (284.5 eV); O1s (530 eV) and V2p (520.5 eV, 513.5 eV).

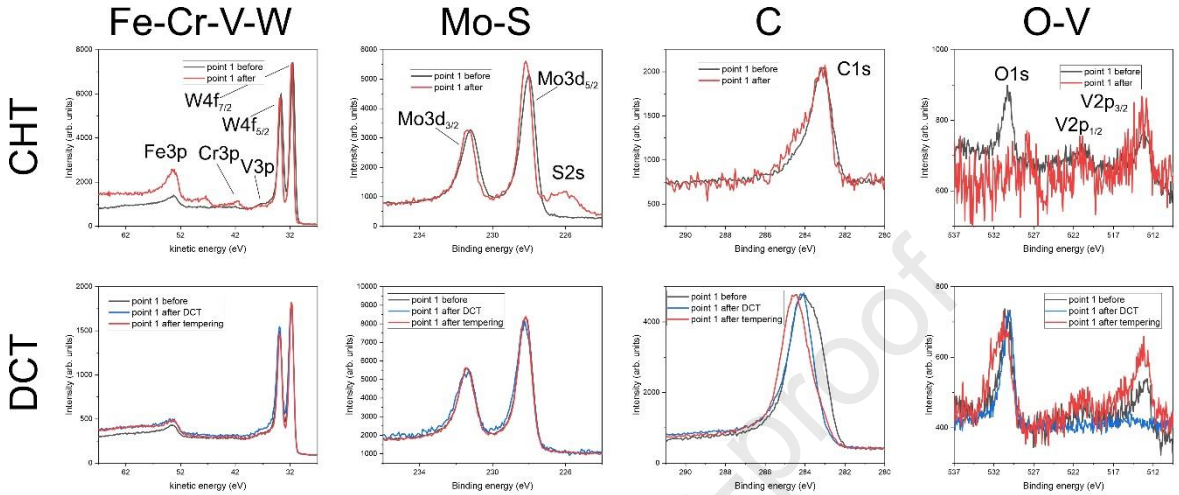

Supplementary material 6: Image series of MOKE macrographs at different externally applied magnetic field for CHT and DCT sample. The field direction and sensitivity axis are provided in the first image of each series. Grey contrast represents no change, whereas bright contrast represents higher change of the magnetization along the sensitivity direction.

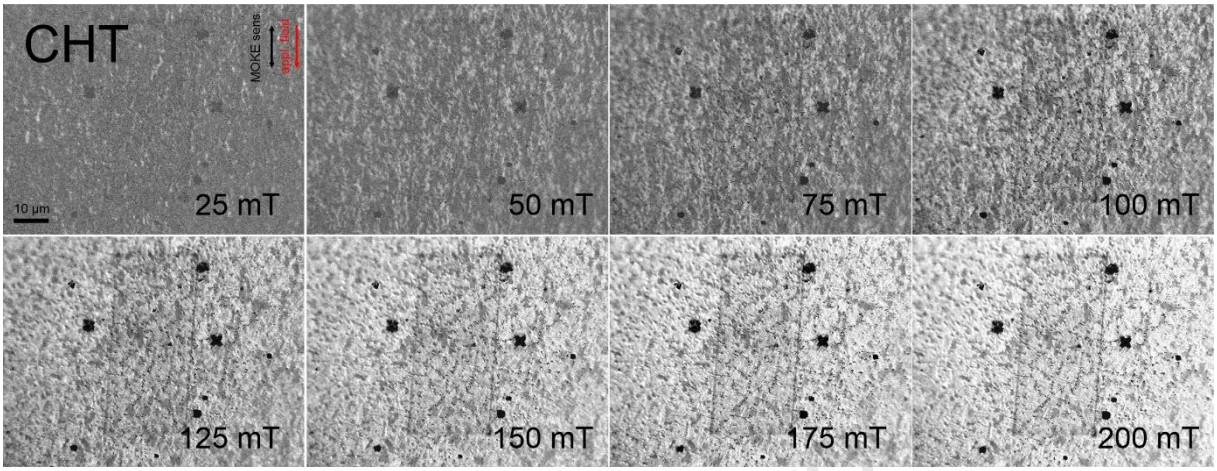

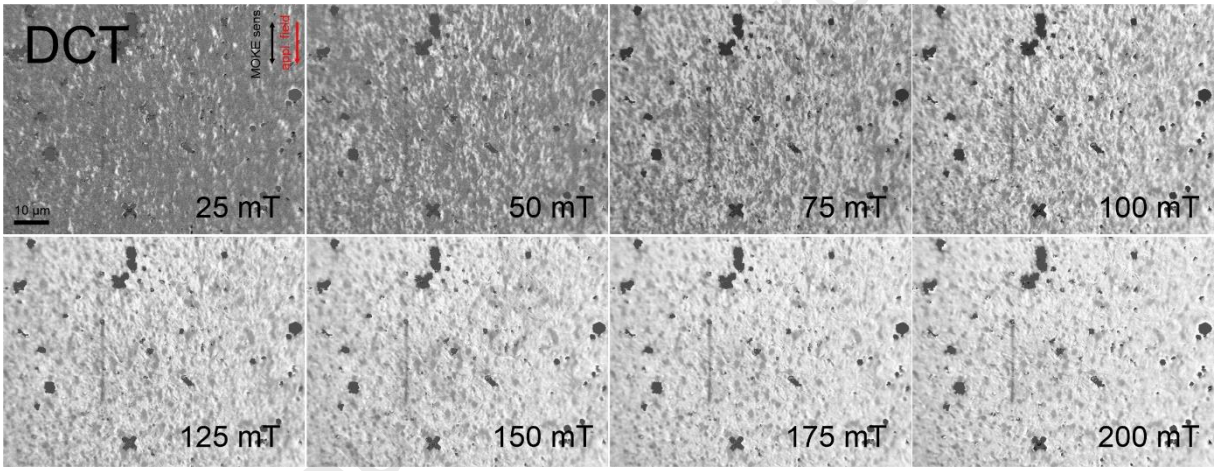

Declaration of interests

☒ The authors declare that they have no known competing financial interests or personal relationships that could have appeared to influence the work reported in this paper.

☐The authors declare the following financial interests/personal relationships which may be considered as potential competing interests: